DOI: https://doi.org/10.14311/TPFM.2025.003

# CFD SIMULATION METHODOLOGY FOR STIRRED VESSELS VALIDATED BY PARTICLE TRACKING VELOCIMETRY

**V. Bílek [1,2], O. Gebouský [1,2], J. Haidl [1], M. Pivokonský [1]**

[1] **Czech Academy of Sciences, Institute of Hydrodynamics, Pod Paťankou 30/5, Prague 160 00, Czech Republic**

[2] **Department of Chemical Engineering, Faculty of Chemical Engineering, University of Chemistry and Technology, Technická 5, Prague 166 28, Czech Republic**

**Abstract**

Stirred vessels are an integral part of many industrial processes. Their design is often based on only experimental data which are limited by available experimental techniques; therefore, their optimisation is usually conducted via a trial-error approach. This study offers a validated CFD simulation methodology that could be used for optimisation and design of industrially relevant stirred vessels. The methodology is based on the RANS model employing the standard $k - \epsilon$ turbulence model and the multiple reference frame approach. The methodology is validated in a vessel that mimics the geometry of a flocculation tank, for which experimental data were also measured using particle tracking velocity and tracer tracking techniques. While the experimental and calculated flow fields show high agreement, simulations of tracer transport within the vessel indicate limitations in the standard approach to the turbulent transport modelling, specifically in the constant value of turbulent Schmidt number.

**Keywords:** stirring, PTV, MRF, CFD

# 1 Introduction

The drinking water treatment includes the coagulation/flocculation process, which removes the majority of impurities in raw water. Within coagulation, destabilisation of the colloidal suspension allows the formation of primary aggregates. Subsequently, flocculation forms larger flocs from the primary aggregates suitable for the following separation technique. The resulting flocs are predominantly affected by hydrodynamic conditions in the flocculation tank.

The hydrodynamic conditions are determined by stirring, which drives the collision frequency of the flocs [1], forming larger flocs. At the same time, the mixing-induced shear stress leads to floc breakage [2], resulting in a reduction in floc size and changes in morphology and shear resistivity [3]. For both flocks' growth and breakage, the magnitude of the shear rate and its distribution in the tank are the key parameters affecting the course of flocculation. Hence, they should be considered when designing and optimizing the industrial flocculation processes [4, 5].

Nowadays, the approach for designing flocculation apparatuses is mainly based on laboratory-scale batch experiments, which provide relatively homogeneous mixing/stirring conditions that can hardly be attained at the industrial scale. A typical mechanically stirred flocculation tank is a large rectangular vessel that houses one or more impellers of various geometries and water flows continuously through the tank; the mean residence time of water in the tank is in order of tens of minutes. Such a design results in zones with slow flow and low shear rate and zones in the impeller vicinity with high flow velocity and high shear rate. Because of this inhomogeneity, the characterisation of the tank's hydrodynamics by simplified integral metrics as the mean-specific power input and the mean residence time can serve only as the tentative design tool. The optimal operating conditions for each flocculation tank must be subsequently determined by trial and error approach [6–8]. To aid this empirical approach, detailed knowledge of local hydrodynamics is essential, allowing for physically sound design and optimisation of flocculation tanks and operating conditions.

To gain insight into the local hydrodynamic conditions in various industrial equipment, computational fluid dynamics (CFD) methods are widely used. In the literature, there are numerous contributions to the modelling of flow in stirred vessels. However, most of those studies examined flow inside a *standard* cylindrical baffled vessel with a centrally mounted impeller, typically a Rushton turbine, which differs significantly from the *non-standard* flocculation tank geometry. Some authors simulated *non-standard* mixed vessel, e.g., Yin [9] and Gun [10], but studies are usually provided without validation of the simulation results. One of the reasons for lacking simulation validation can be the scarcity of experimental data for *non-standard* geometries.

This study reacts to this unsatisfactory situation and aims to offer a reliable, experimentally verified methodology for the simulation of flow in *non-standard* vessels; attention is paid to the industrial potential of the methodology, which means affordable computational costs and high mesh structure versatility. The methodology foundation was laid in the study of Idžakovičová [11], critically reviewing existing modelling approaches and providing the verified framework for simulating the *standard* vessel with the Rushton turbine. This work extends the methodology by adding recommendations for unstructured mesh generation and validates the methods on experimental data obtained within the work using particle tracking velocimetry (PTV). Both simulations and experiments were performed for a pilot-scale geometry (200 L) and conditions that mimic the environment of industrial flocculation tanks.

## 2 Mathematical model

**Fluid dynamics modelling** The mathematical model framework is drawn from the study Idžakovičová [11]. The methodology is based on the Reynolds-Averaged Navier-Stokes equations (RANS) with a critically chosen standard $k - \epsilon$ turbulence model [12] that meets relatively low computational demands and provides a sufficiently accurate flow field in the *standard vessel* [11]. The impeller rotation is integrated via the multiple reference frame (MRF) approach. The resulting equations are of the form

$$\begin{aligned} \nabla \cdot (\overline{\boldsymbol{U}} \otimes \overline{\boldsymbol{U}}_{\mathrm{R}}) + \boldsymbol{\Omega} \times \overline{\boldsymbol{U}} &= -\frac{\nabla \overline{p}}{\rho} + \nabla \cdot \left[(\nu + \nu_{\mathrm{t}}) \nabla \overline{\boldsymbol{U}}\right], \\ \nabla \cdot \overline{\boldsymbol{U}} &= 0\,, \end{aligned} \tag{1}$$

where $p$ is the pressure, $\rho$ density, $\boldsymbol{U}$ and $\boldsymbol{U}_{\mathrm{R}}$ are the absolute velocity in the inertial frame and the relative velocity in the rotating frame, respectively. Next, $\boldsymbol{\Omega}$ is the angular velocity of the frame relative to the stationary frame, and $\boldsymbol{U} = \boldsymbol{U}_{\mathrm{R}} + \boldsymbol{\Omega} \times \boldsymbol{r}$ with $\boldsymbol{r}$ being the position vector. The bars over the symbols denote the Reynolds-averaged variables. Lastly, $\nu_{\mathrm{t}}$ is the turbulent viscosity provided by the standard $k - \epsilon$ model, and $\nu$ is the kinematic viscosity.

**Tracer transport modelling** The tracer transport utilises the advection-diffusion equation in the form

$$\frac{\partial c}{\partial t} + \nabla \cdot \left(\overline{\boldsymbol{U}} c\right) = \nabla \cdot \left[(D + D_{\mathrm{t}}) \nabla c\right] , \tag{2}$$

where $c$ is tracer concentration, $t$ is time, $\overline{\boldsymbol{U}}$ is velocity vector calculated from the flow simulation, $D$ and $D_{\mathrm{t}}$ are the molecular and the turbulent diffusivity, respectively. The turbulent diffusivity is obtained from

$$D_{\mathrm{t}} = \frac{\nu_{\mathrm{t}}}{\mathrm{Sc}_{\mathrm{t}}}, \tag{3}$$

where $\mathrm{Sc}_{\mathrm{t}}$ is the turbulent Schmidt number, usually handled as a constant [13]. Based on the review of Gualtieri [14] and the findings of Idžakovičová [11], the value of $\mathrm{Sc}_{\mathrm{t}} = 0.7$ was used.

**Boundary and initial conditions** The working fluid is water at 20 °C ($\nu \approx 10^{-6}\,\mathrm{m}^2\,\mathrm{s}^{-1}$). The computational domain comprises boundaries that represent tank walls, a lid, and an impeller. The no-slip boundary condition for velocity and the zero-gradient boundary condition for pressure and concentration were imposed for all boundaries. The near-wall behaviour of turbulence quantities ($k$, $\epsilon$, $\nu_t$) was handled with the standard wall functions [15]. The flow simulations were initialised with the fluid being at rest, zero pressure and constant values of 0.3 $\mathrm{m}^2\mathrm{s}^{-2}$, 14.8 $\mathrm{m}^2\mathrm{s}^{-3}$, and 0 $\mathrm{m}^2\mathrm{s}^{-1}$ for $k$, $\epsilon$, and $\nu_{\mathrm{t}}$, respectively. When calculating tracer transport, the initial concentration was set to 0 except for the regions that represent the initial injection of tracer in experiments where the initial concentration of 1 was prescribed. Both tracer inlet regions were hemispheres ($\approx 40\,\mathrm{mL}$) located on the rear wall - see Fig. 1.

**Solving methods** Calculations were performed using OpenFOAM v10 [16]. The Eq. (1) were solved by the SIMPLE algorithm implemented in the *simpleFoam* solver. If there were problems with simulation convergence, the simulation strategy was changed to the pseudo transient local time stepping (LTS) method, using the PISO algorithm and *pimpleFoam* solver. The second-order upwind scheme was used for the divergence discretisation, and the second-order linear schemes were employed for gradient and Laplacian discretisation.

The tracer transport Eq. (2) was solved using a modified *scalarTransportFoam* solver from the OpenFoam library, which accounts for the turbulent diffusivity calculated using Eq. (3). The time step was chosen to limit the maximal Courant number below 0.95.

**Evaluation metrics** The simulation validation was performed by comparing simulation results with experimental data. Specifically, the quantities of interest are the averaged velocity field, the turbulence kinetic energy, $k$, distribution, and time of 95 % tracer homogenisation degree, $\theta_{95}$. The turbulence kinetic energy was calculated from the obtained 2D PTV data, assuming turbulence isotropy

$$k = \frac{1}{2}(U_x'^2 + U_y'^2 + U_z'^2) \approx \frac{3}{4}\left(U_x'^2 + U_y'^2\right). \tag{4}$$

The $\theta_{95}$ values were evaluated as the time necessary for the concentration coefficient of variance

$$CoV\,(t) = \frac{1}{\bar{c}\,(t)}\sqrt{\frac{1}{V_T}\sum_{i=1}^{N_c} V_i(c_i\,(t) - \bar{c}\,(t))^2} \tag{5}$$

decreases below the threshold value of 0.05 [17]. In Eq. (5), $c_i$ represents the actual concentration in $i$-th cell, $\bar{c}$ marks average concentration in the tank, $V_i$ is $i$-th cell volume and $V_T$ is the tank volume. In terms of the independence of the mesh size, a power number $\mathrm{Po} = {}^{P}/_{\rho N^3 D^5}$ and a pumping number $\mathrm{N_Q} = {}^{Q}/_{ND^3}$ are compared, where $P$ is a power, $N$ is the impeller speed, $D$ is the impeller diameter and $Q$ is an internal circulation calculated as $Q = \iint_{A_1 \cup A_2} \overline{\mathbf{U}} \cdot \mathrm{d}\mathbf{A}$, with $A_1$ and $A_2$ being the circular surfaces placed 1 mm on and under the edges of the impeller blades and having a diameter of $D$.

## 3 Geometry and computational mesh design

The geometry of interest, sketched in Fig. 1 comprises the rectangular tank with an asymmetrically placed Rushton turbine. The vessel design and used mixing intensity are inspired by stirred flocculation tanks used in drinking water treatment facilities. The width of the blades and the disc of the Rushton turbine was 4.33 mm.

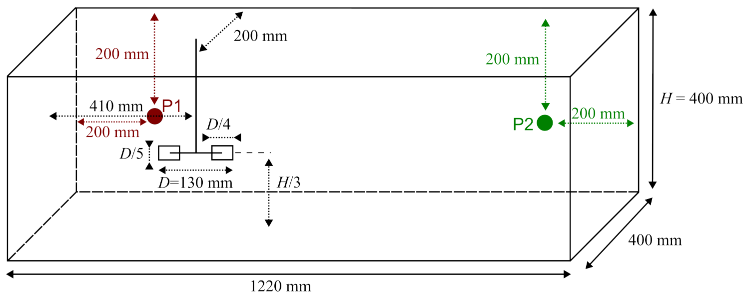


**Figure 1:** Configuration of the asymmetric tank equipped with the Rushton turbine, P1 and P2 denote locations of injection ports

The computational mesh is based on recommendations from the study of Idžakovičová [11]. The resulting mesh consists of 2.67 million cells. The characteristic cell size is 2 mm in the vicinity of the impeller and 5 mm elsewhere. The mesh consists of two main parts; the cylinder designed as the o-mesh with the impeller placed inside the central rectangular block, which provides a suitable mesh for the MRF. The mesh is created using the *snappyHexMesh* utility, resulting in mostly structured hexahedral mesh with arbitrary polyhedral cells in the impeller's vicinity and transition between parts. The left half of the generated mesh is shown in Fig. 2. The main mesh quality metrics are listed in Table 1. The MRF zone is a perfect cylinder and six cells separate the MRF boundary from the stitched transition between the mesh parts.

**Table 1:** The mesh quality metrics of the asymmetric tank

| no. cells | max. non-ortho | avg. non-ortho | max. skewness | max. aspect ratio |
|---|---|---|---|---|
| 2.67 mil | 65.9 | 8.13 | 2.48 | 8.45 |

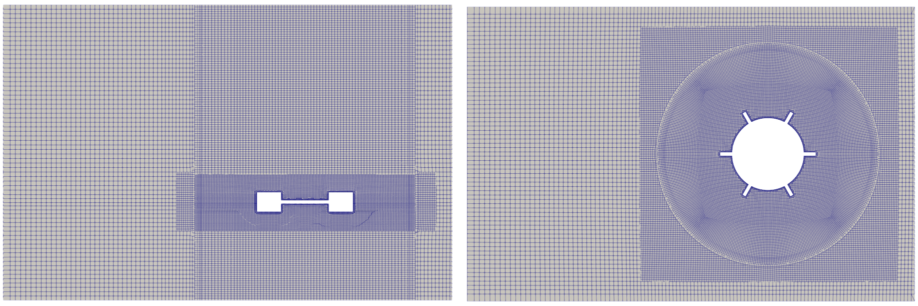

**(a)** Side view **(b)** Top view
**Figure 2:** Generated mesh for asymmetric tank; only left half of the tank

# 4 Experimental

**Particle Tracking Velocimetry** Experimental data for the flow field validation were obtained using the 2D PTV technique. As seeding particles, Acrylonitrile Butadiene Styrene (ABS) granules with a density of $1080\,\mathrm{kg\,m^{-3}}$ and characteristic dimensions ranging from 0.4 to 0.6 mm were used. The sodium dodecyl sulphate solution at a concentration of 0.025 g / L was used to suppress the particle aggregation. The mean sedimentation velocity of the particles of $5\,\mathrm{mm\,s^{-1}}$ was reflected in the evaluation of the PTV data. The size of the particles is of the same order of magnitude as the turbulence Kolmogorov length scale $({}^{\nu^3}/{}_{\epsilon})^{1/4}$ everywhere except the the highly turbulent region in the impeller proximity.

The PTV data are measured in a continuously illuminated plane created by an in-house assembled laser sheet of thickness of 6 mm, using green laser modules (505 nm) of a total output power of 240 mW. For image capture, the Dantec Dynamics SpeedSense VEO CCD high-speed camera with a spatial resolution of 1280×800 px was used. Each measurement consisted of 30 s, i.e., 30 000 frames were taken.

Measurements were carried out for 2 impeller speeds (2.2 and 3.45 rps) and 4 planes; three front view planes were located 5 cm, 10 cm, and 15 cm in front of the shaft, and one side view plane located 1 cm in front of the shaft on the side closer to the side wall. To increase the measurement's spatial resolution and light intensity of the laser sheet, the front-view measurements were performed individually for the left and right half of the tank.

In data evaluation, the raw images were masked to eliminate noisy parts of the image (walls, impeller), and the white threshold of 50/255 was applied to distinguish between particles and background noise. The prepared images were evaluated using the TracTrac [18] software to identify individual particles and track their trajectories. The TracTrac software identifies and labels the illuminated particles present in three or more consequent images. Moreover, it filters the static (false) signals. The evaluated data contain the labels and coordinates of the particles and the sequence of frame numbers in which they were detected. Finally, the data evaluated by the TracTrac data were processed with a custom-made code that provides perspective correction and coordinate transformation from px to mm, trajectory filtering and sorting, velocity calculation, and visualisation of the results. After data processing, only particle trajectories that meet the following requirements are considered valid:

1. The trajectory must not have consecutive points in a distance longer than 3 mm which limits the maximal particle velocity evaluated from the images to 3 m/s (approx. two times the impeller speed)
2. The trajectory must travel at least a distance of 0.6 mm that corresponds to a distance of one px, thus ignoring a subpixel motion.
3. Only trajectories with travelled distance at least 2 mm or having 10 or more points are processed.

To calculate the velocity corresponding to each trajectory, the temporal changes of the particle's coordinates $(x(t), y(t))$ are fitted with straight lines with $U_x$, $U_y$ being their slopes.

In the final processing phase, the entire measured domain was divided into subdomains representing $1\,\mathrm{cm}^2$ of the view, and individual trajectories were assigned to respective subdomains based on trajectory centre; trajectories, which passed more than two subdomains were divided into shorter ones and assigned to their respective subdomains. For each subdomain, the mean velocity $\left(\overline{U}_x, \overline{U}_y\right)$ and the kinetic turbulence energy $k$ were calculated. The calculation of $k$ is based on Eq. (4), and its application on the experimental data takes the form

$$k \approx \frac{3}{4N} \sum_{i=1}^{N} \left(U_{x,i} - \overline{U}_x\right)^2 + \left(U_{y,i} - \overline{U}_y\right)^2 . \tag{6}$$

Note that trajectories with a difference in the subdomain's mean velocity larger than 4 times the velocity standard deviation were removed from the valid data as outliers. Typically, each subdomain included hundreds of trajectories. Each trajectory consisted of dozens of points corresponding to a measurement error of about $1.5\ \mathrm{cm\,s^{-1}}$.

**Tracer homogenisation measurements** Homogenisation experiments were performed using colorimetric and conductometric techniques, following the methodologies of Gebouský [19**?** ]. For the colorimetric measurements, the decolorization technique with the iodine-starch-sodium thiosulfate system was employed. The conductometric experiments used the dispersion of the NaCl solution injected into the deionised water. The experiments were carried out in triplicate for two locations of tracer injection (see Fig. 1), and both used impeller speeds. The resulting homogenisation times are presented as the average of both conductometric and colorimetric measurements.

## 5 Results and discussion

**PTV methodology validation** The repeatability of the PTV measurements was assessed by comparing data from two independent measurements; in Fig. 3, the velocity profiles are compared in the plane perpendicular to the front wall at distance 15 cm. Both data sets are almost identical, and the main flow features, such as velocity distribution and location of flow structures, are in great agreement. Only small discrepancies are present; the flux pumped into the impeller from the upper right side has a slightly different direction, the large eddy on the left side has a slightly different position, and the separation zone on the left bottom side is shifted about 50 mm. Due to this agreement between data, the PTV methodology is considered relevant and reliable for assessing RANS simulation results.

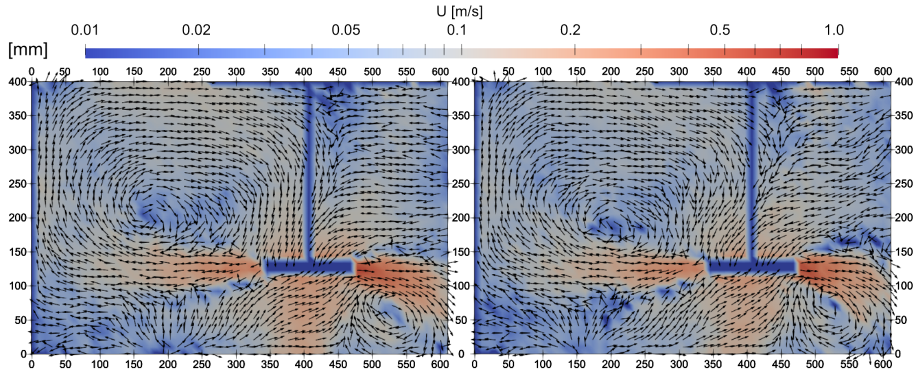


**Figure 3:** The comparison of velocity profiles between independent PTV data, front plane 5 cm in front of the shaft, left side, 2.2 rps

**Mesh size independence study** The mesh size independence study was performed via flow field calculation with a denser mesh (5.47 million cells). The results of both simulations were compared in terms of impeller power and pumping numbers. For the coarser and finer meshes, the power numbers of 3.60 and 3.57 were calculated. In both cases, the pumping number of 0.59 was attained. In addition, a visual comparison of the calculated flow fields (flow direction and velocity, position of vortex structures, distribution of turbulence kinetic energy) confirmed that the coarser mesh is sufficient to provide insight into the tank hydrodynamics.

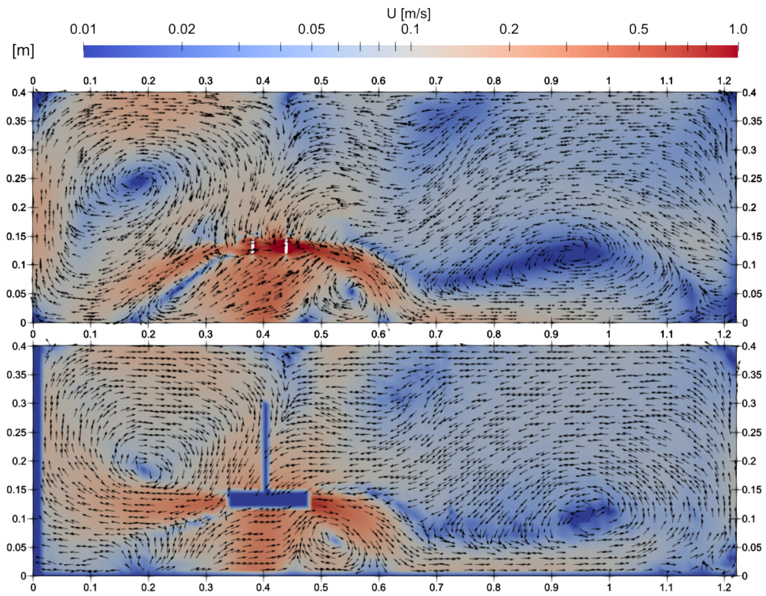


**Figure 4:** The comparison of velocity profiles between the RANS results (upper) and the PTV data (lower), the front plane 5 cm in front of the shaft, 3.45 rps

**Comparison between PTV experiments and simulation** Generally, by comparing PTV and RANS simulations, the main flow characteristics are present in both datasets; however, the comparison revealed some variances in their exact location and shape. Looking at the velocity distribution presented in Fig. 4, the results have much in common, and only a few deviations are present. The main left eddy has different shapes and positions, and the streams pumped out of the impeller are broader for PTV results. The comparison of the predicted and measured turbulence kinetic energy shown in Fig. 5 confirms the findings made for velocity fields. Although some differences are apparent, the distribution and magnitude of $k$ in different parts of the tank are in mutual agreement. Although $k$ is not directly related to the flocculation modelling, the success of its prediction suggests the ability of the often condemned $k - \epsilon$ model to characterise turbulent quantities. From these, the dissipation rate of the kinetic energy of turbulence $\epsilon$ is of the main interest, as it is directly related to the shear rate magnitude, the key factor in the growth and breakage of the flocs [2].

**Tracer transport experiments** The tracer transport, evaluated as the tracer homogenisation time, indicates the simulation reliability in predicting the trajectories of substances and flocs through the flocculation tank. The results of the simulated course of homogenisation – the development of tracer concentration $CoV$ – are compared with the experimental data on the homogenisation time $\theta_{95}$. The comparison is shown in Fig. 6. Apparently, the simulations performed with the generally recommended value of $\mathrm{Sc_t} = 0.7$ underestimated the homogenisation time by 25%-35%. To match the simulation and experimental results, the $\mathrm{Sc_t}$ was optimised to 1.8 for which the simulation results agree within 10% with the experimental data for the impeller speed $N = 2.2$ s$^{-1}$. However, when the optimised value was used for the simulation of the vessel stirred at a higher speed of $N = 3.45$ s$^{-1}$, the differences exceeding 20% were again achieved.

These results may indicate shortcomings in the tracer transport modelling on top of flow fields calculated via the RANS approach. This observation is further supported by a literature review, which yields the range of "optimal" $\mathrm{Sc_t}$ values from 0.1 to 2, often optimised for a particular geometry or simulation case Gualtieri [14]. Alternatively, the dependence of $\mathrm{Sc_t}$ on local hydrodynamic conditions was suggested by Salzano [21]. Apparently, the commonly used approach to the turbulent transport characterisation and its impact on the RANS simulation potential for industrial

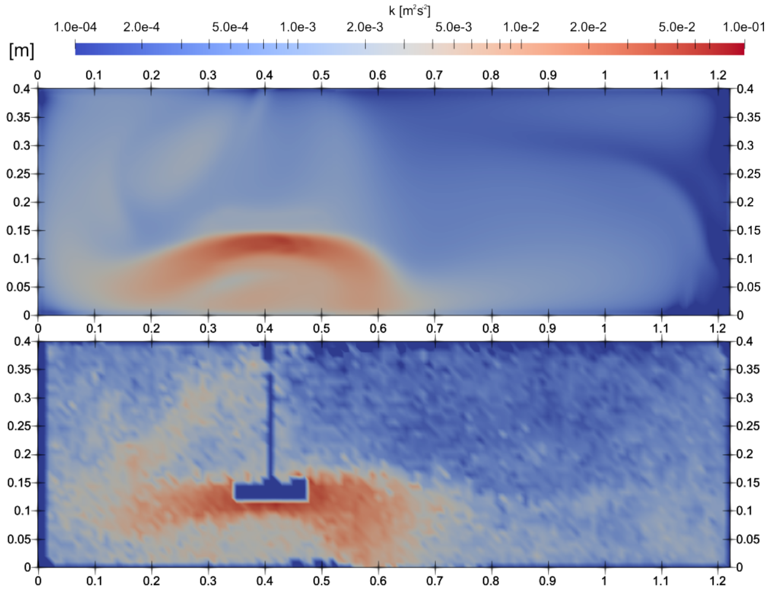


**Figure 5:** The comparison of turbulence kinetic energy between the RANS results (upper) and the PTV data (lower), the front plane 10 cm in front of the shaft, 2.2 rps

flocculation modelling require further research.

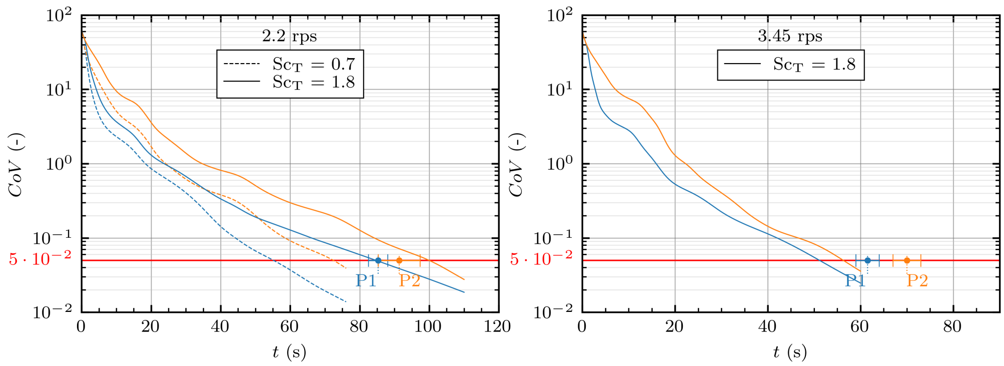


**Figure 6:** Comparison of homogenisation times between the experiments and the tracer transport simulations for two impeller speeds: 2.2 rps and 3.45 rps

# 6 Conclusions

This contribution validates the methodology developed to simulate hydrodynamic conditions in *non-standard* industrial tanks such as flocculation tanks. The simulation methodology, based on the study of Idžakovičová [11], is designed to meet the requirement of relatively low computational demands and the flow resolution sufficient for industrial applications. It is based on the RANS approach, employing the standard $k - \epsilon$ turbulence model and the MRF approach for impeller rotation. The results of the simulations performed with the developed methodology were validated using PTV measurements of the flow field in the rectangular pilot-plant stirred tank ($V$ = 200 L). While sufficient agreement was found for the simulated and experimental flow fields, unexpected weaknesses are revealed in describing the tracer transport on top of RANS simulations. Based on the results presented in this work, $Sc_t$ does not seem to be a constant as is usually assumed but depends on local hydrodynamic conditions. This topic and its impact on the potential of CFD for physically sound and reliable modelling of industrial flocculators should be investigated in the following studies.

**Acknowledgment**

The work on this paper was supported by the institutional support RVO:67985874 and by the Czech Academy of Sciences Premium Academiae. Special thanks belong to Strategy AV21 of the Czech Academy of Sciences (VP20 – Water for life). The participation of VB and OG was financially supported by the grant of Specific University Research A1_FCHI_2024_004. Computational resources were provided by the e-INFRA CZ project (ID:90254), supported by the Ministry of Education, Youth and Sports of the Czech Republic.

# References

[1] Essemiani, K. & de Traversay, C.: Optimisation of the flocculation process using computational fluid dynamics. *Chemical Water and Wastewater Treatment VII*, IWA Publishing (2002), pp. 41–49.

[2] Šoóš, M. & Moussa, A. S. & Ehrl, L. & Sefcik, J. & Wu, H. & Morbidelli, M.: Effect of shear rate on aggregate size and morphology investigated under turbulent conditions in stirred tank. *Journal of Colloid and Interface Science*, vol. 319, no. 2: (2008) pp. 577–859.

[3] Prat, O. P. & Ducoste, J. J.: Modeling spatial distribution of floc size in turbulent processes using the quadrature method of moment and computational fluid dynamics. *Chemical Engineering Science*, vol. 61, no. 1: (2006) pp. 75–86.

[4] Goula, A. M. & Kostoglou, M. & Karapantsios, T. D. & Zouboulis, A. I.: A CFD methodology for the design of sedimentation tanks in potable water treatment: Case study: The influence of a feed flow control baffle. *Chemical Engineering Journal*, vol. 140, no. 1-3: (2008) pp. 110–121.

[5] Bridgeman, J. & Jefferson, B. & Parsons, S. A. : Computational fluid dynamics modelling of flocculation in water treatment: A review. *Engineering Applications of Computational Fluid Mechanics*, vol. 3, no. 2: (2009) pp. 220–241.

[6] Pivokonský, M. & Vašatová, P. & Načeradská, J. & Pivokonská, L.: Koagulace při úpravě vody: teorie a praxe, Academia (2020).

[7] ČSN 75 5201: Navrhování úpraven vody, Praha, Úřad pro technickou normalizaci, metrologii a státní zkušebnictví, 2023.

[8] Bratby, J.: Coagulation and flocculation in water and wastewater treatment, IWA Publishing (2016).

[9] Yin, C. & He, J. & Xiong, Y. & Zhang. Z & Luo, X. & Shu, Y. & Long, D. & Zheng K.: Improved suspension quality and liquid level stability in stirred tanks with Rotor-Stator agitator based on CFD simulation. *Particuology*, vol. 82: (2023) pp. 64–75.

[10] Gun, S. & Chatterjee, S. & Hens, A.: CFD based analysis of chlorination contact tank design. *Materials Today: Proceedings*, vol. 87: (2022) pp. 1813–1818.

[11] Idžakovičová, K. & Bílek, V. & Haidl, J. & Isoz, M. & Pivokonský, M.: Flow Simulations Approach for Flocculation Tanks. *Topical Problems of Fluid Mechanics* (2024) pp. 77–84.

[12] Launder, B. E. & Spalding, D. B.: The numerical computation of turbulent flows. *Numerical prediction of flow, heat transfer, turbulence and combustion*, Elsevier (1983), pp.96–116.

[13] Käpylä, P. J. & Singh, N. K.: Turbulent Prandtl number from isotropically forced turbulence. *Journal of Fluid Mechanics*, vol. 952: (2022).

[14] Gualtieri, C. & Angeloudis, A. & Bombardelli, F. & Jha, S. & Stoesser, T.: On the Values for the Turbulent Schmidt Number in Environmental Flows. *Fluids*, vol. 2, no. 2: (2017).

[15] Moukalled, F. & Darwish M.& Mangani, L.: The finite volume method in computational fluid dynamics: an advanced introduction with OpenFOAM and Matlab. Elsevier (2016).

[16] The OpenFOAM Foundation Ltd, Openfoam v10, 2022. URL: https://openfoam.org/version/10/, last accessed 03/2024.

[17] Paglianti, A. & Carletti, C. & Busciglio, A. & Montante, G.: Solid distribution and mixing time in stirred tanks: The case of floating particles. *The Canadian Journal of Chemical Engineering*, vol. 95, no. 9: (2017) pp. 1789–1799.

[18] Heyman, J.: Solid distribution and mixing time in stirred tanks: TracTrac: A fast multi-object tracking algorithm for motion estimation. *Computers and Geosciences*, vol. 128: (2019) pp. 11–18.

[19] Gebouský, O. & Haidl, J. & Bodnár, J. & Pivokonský, M.: Improvement of an Unbaffled Stirred Tank Mixing Characteristics Using Variable Speed Impeller. *Topical Problems of Fluid Mechanics* (2024).

[20] Gebouský, O. & Idžakovičová, K. & Haidl, J.: Mixing characteristics of unbaffled bioreactor with levitating radial impeller. *Chemical Engineering Science*, vol. 276: (2023).

[21] Salzano, F. & Gualtieri, C.: The effect of baffle spacing on hydrodynamics and solute transport in serpentine contact tanks. *Journal of Hydraulic Research*, vol. 52, no. 1: (2014) pp. 152–154.